Vision, Modeling, and Visualization (2016)
M. Hullin, M. Stamminger, and T. Weinkauf (Eds.)

Singularities of the Inertial Flow Map Gradient

Tobias Günther[1] and Holger Theisel[2]

[1]Computer Graphics Laboratory, ETH Zurich
[2]Visual Computing Group, University of Magdeburg

Abstract

Inertial particles are finite-sized objects that are carried by flows, for example sand particles in air. In contrast to massless tracer particles, the trajectories of inertial particles can intersect in space-time. When this occurs, the inertial flow map gradient becomes singular. This has an impact on visualization concepts that require the flow map gradient to be invertible. An example are influence curves, which allow to move inertial particles backward in time and thereby avoid the numerically ill-posed inertial backward integration. In this paper, we show that singularities of the inertial flow map gradient can act as poles for influence curves, i.e., as structures that influence curves cannot cross. Influence curves thereby decay into disconnected pieces. We extract singularities in space-time and propose a simple approach to extract influence curves even when they are spatially disconnected. We demonstrate the extraction techniques and discuss the role of singularities in a number of 2D vector fields.

Categories and Subject Descriptors (according to ACM CCS): I.3.3 [Computer Graphics]: Picture/Image Generation—Line and curve generation

1. Introduction

Traditionally, flow visualization is concerned with the observation of massless particles. Since they follow the flow perfectly tangential, they are an expressive tool to visualize the behavior of the flow. In many engineering problems, however, domain scientists are not directly interested in the flow itself, but rather in the motion of finite-sized objects that are carried with the flow, such as sand stirring during helicopter landing [SGL10, SBL11, KGRK14], plankton movement in jellyfish feeding [PD09, SPH11] or droplets in meteorology [SRCV98, SH09, Bor11]. These so-called *inertial particles* behave differently than massless particles, and have thus recently gained attention in the visualization community. For instance, it was shown that inertial particles swirl around different vortex corelines [GT14] and that in terms of topology an inertial particle is everywhere subject to attraction [GT16b], which makes inertial backward integration numerically ill-posed [GT16c].

In this paper, we investigate another fundamental difference to massless particles: The trajectories of massless particles will never intersect in space-time; with inertial particles, however, they can. Imagine three inertial particles, released infinitesimal close to one another in a 2D flow. They span a triangle, which deforms over the course of the advection. Due to inertia effects, the paths of inertial particles might cross in space-time. In this case, the triangle flips orientation. For a brief moment its area is zero. Thereby, the three points are collinear or (even rarer) they collapse shortly to a point.

As we will show, the intersections of inertial pathlines can be determined as singularities of the inertial flow map gradient, i.e., as locations where one of the eigenvalues of the inertial flow map gradient becomes zero. The locations can thus be extracted as the union of the eigenvalues' zero-level isosurfaces. Locating and understanding these singularities has impact on visualization concepts that require the inverse of the flow map gradient [WT10, GT16c]. Influence curves [GT16c] for instance, are curves from which an inertial pathline integration leads to the same observation point. They can be used to integrate inertial particles backward in time [GT16a], which solves the source inversion problem, i.e., recovers the source of airborne or waterborne pollution. Due to the strongly attracting nature of the inertial phase space, this is a numerically challenging problem [MBZ06, HS08]. We will show that under certain conditions, singularities of inertial flow map gradients can act as poles, i.e., influence curves do not cross them. Since influence curves may exist on both sides of a pole, they decay into multiple disconnected pieces; an integration-based computation could only extract a single piece. To overcome this problem, we propose a simple approach to extract influence curves in all parts of the domain, which, however, requires discretization.

2. Background and Related Work

The following section introduces into the modeling of inertial particles and reviews recent work on inertial particles in visualization.

DOI: 10.2312/vmv.20161344

2.1. Motion of Inertial Particles

The motion of small spherical particles is subject to a number of forces, which have been combined into the Maxey-Riley equations [MR83]. See Farazmand and Haller [FH15] for a recent review of improvements and properties of the model. In many applications, assumptions can be made, which lead to simplified equations of motion. For instance, Crowe et al. [CST98] described a model that assumes small particles with a density much higher than the density of the surrounding air. Even though particle collisions are not treated, we will see that they have nevertheless an impact on the numerical extraction of derived quantities and curves. Due to accumulating inertia effects, inertial particles not only have a position, but also a velocity state to keep track of. For an underlying time-dependent vector field $\mathbf{u}(\mathbf{x}, t)$, both rates of changes are modeled together in a higher-dimensional vector field [GT14]:

$$\frac{\mathrm{d}}{\mathrm{d}\tau}\begin{pmatrix}\mathbf{x}\\ \mathbf{v}\\ t\end{pmatrix} = \begin{pmatrix}\mathbf{v}\\ \frac{\mathbf{u}(\mathbf{x},t)-\mathbf{v}}{r}+\mathbf{g}\\ 1\end{pmatrix} \text{ with } \begin{pmatrix}\mathbf{x}\\ \mathbf{v}\\ t\end{pmatrix}(0) = \begin{pmatrix}\mathbf{x}_0\\ \mathbf{v}_0\\ t_0\end{pmatrix} \tag{1}$$

where $\mathbf{g}$ is a gravity vector (w.l.o.g. we set $\mathbf{g} = \mathbf{0}$) and $\mathbf{x}_0$, $\mathbf{v}_0$, t_0 are the initial particle position, velocity and time. Thereby, r is the particle response time, which is a mass-dependent parameter that is characterized by particle diameter d_p, particle density ρ_p and the viscosity μ of the surrounding air:

$$r = \frac{d_p^2\,\rho_p}{18\mu} > 0 \tag{2}$$

Throughout the paper, we set the particle density to $\rho_p = 1600\,kg/m^3$, which corresponds to dry sand and assume the surrounding medium to be air. Thus, the viscosity was set to $\mu = 1.532{\cdot}10^{-5}\,kg/(m{\cdot}s)$. If not mentioned otherwise, the diameter was set to $d_p = 200\,\mu m$.

2.2. Inertial Flow Map and its Derivatives

The flow map is a commonly-used concept that maps a particle to its destination after integration for a certain duration. Following [GKKT13], we define the flow map $\phi(\mathbf{x}, \mathbf{v}_0, t_0, \tau)$ as a function that maps a particle seeded at $\mathbf{x}$ with initial velocity $\mathbf{v}_0$ at time t_0 to the spatial location that is reached after duration τ. Note that for the remainder of this work, we assume $\mathbf{v}_0$ and t_0 to be constant for all considered particles. (This is common practice in Lagrangian measures, for instance in inertial FTLE, see Section 2.3.)

In an n-dimensional flow, the spatial gradient of the inertial flow map $\phi_\mathbf{x} = \frac{\mathrm{d}\phi(\mathbf{x},\mathbf{v}_0,t_0,\tau)}{\mathrm{d}\mathbf{x}}$ is an $n \times n$ matrix that characterizes the behavior of nearby-released inertial particles. In traditional steady massless flows, the flow map gradient is always positive-definite, except for discretization artifacts. In the inertial case, the flow map gradient might as well without discretization become negative-definite, indefinite or even singular, since trajectories can intersect.

2.3. Inertial Particles in Visualization

Observations of inertial particles in fluid flows pose new challenges, since particle motion is governed by a higher-dimensional vector field. Early examples of inertial particle visualizations were created by Roettger et al. [RSBE01], who visualized sand particle concentration on cars via heat maps in order to determine soiling. Sapsis et al. [SH09, SPH11] and Peng et al. [PD09] computed finite-time Lyapunov exponents for inertial particles. Inertial FTLE was calculated by Raben et al. [RRV14] from measured inertial trajectories and Sudharsan et al. [SBR15] studied the relation between inertial preferential particle settling and massless FTLE. Aside from calculating inertial FTLE based on the spatial separation only, separation has also been considered in the spatio-velocity domain [GPPMn15]. Recently, Sagristà et al. [SJJ*16] investigated the spatial and velocity subspaces of phase space FTLE, and studied the spatial folding of inertial flow maps by *multiplicity maps*.

In another thread of research, the motion of finite-sized objects in fluid flows has been studied by the use of integral geometry [GKKT13] in the air flow around a helicopter in forward flight close to a sediment bed. Later, Günther and Theisel extracted inertial vortex corelines [GT14] and visualized the separation behavior of inertial particles due to varying response time (mass) [GT15]. More recently, they looked into inertial vector field topology for underlying steady 2D flows [GT16b]. They conducted a full classification of the isolated critical points that may arise in the inertial phase space. A direct backward integration in Eq. (1) is not possible, as the inertial phase space exhibits strong repelling behavior [MBZ06, HS08, GT16b], which makes the backward integration numerically ill-posed.

To overcome this problem, Günther and Theisel [GT16c] recently proposed *influence curves*. These curves allow to move inertial particles backward in time, which can be applied to calculate inertial backward FTLE [GT16a]. An influence curve $\mathbf{c}(\mathbf{x}, \tau)$ is the union of all points from which an inertial pathline integration, starting at time t_0 with initial velocity $\mathbf{v}_0$, will terminate in $\mathbf{x}$:

$$\phi(\mathbf{c}(\mathbf{x}, \tau), \mathbf{v}_0, t_0, \tau) = \mathbf{x} \tag{3}$$

The curves are parameterized by the integration duration τ, and can be computed as tangent curves of the vector field [GT16c]:

$$\mathbf{h}(\mathbf{x}, t) = -\phi_\mathbf{x}^{-1}\left[\phi_\mathbf{v}\left(\frac{\mathbf{u}(\mathbf{x}, t_0)-\mathbf{v}_0}{r}+\mathbf{g}\right)+\phi_t\right]-\mathbf{v}_0 \tag{4}$$

The tangent curve-based extraction requires the inverse of the inertial flow map gradient, thus the technique only works well as long as the inertial flow map gradient stays positive definite. In this paper, we examine more closely the role of singularities in the extraction process and propose a simple technique to approximate influence curves.

3. Singularities of the Inertial Flow Map Gradient

The inertial flow map gradient $\phi_\mathbf{x}$ is a matrix that characterizes the behavior of nearby-released inertial particles. In inertial flows, it can be *singular*, i.e., the determinant is zero, when inertial trajectories cross in space-time, see Fig. 1 for example. For a given initial velocity $\mathbf{v}_0$ and start time t_0, these are locations $(\mathbf{x}, \tau)$ in space-time (whereas τ denotes the integration duration) with

$$\det(\,\phi_\mathbf{x}(\mathbf{x}, \mathbf{v}_0, t_0, \tau)\,) = 0 \tag{5}$$

In this paper, we call such event a *singularity*. The term is usually interchangeably used for critical points, but not here. In an n-

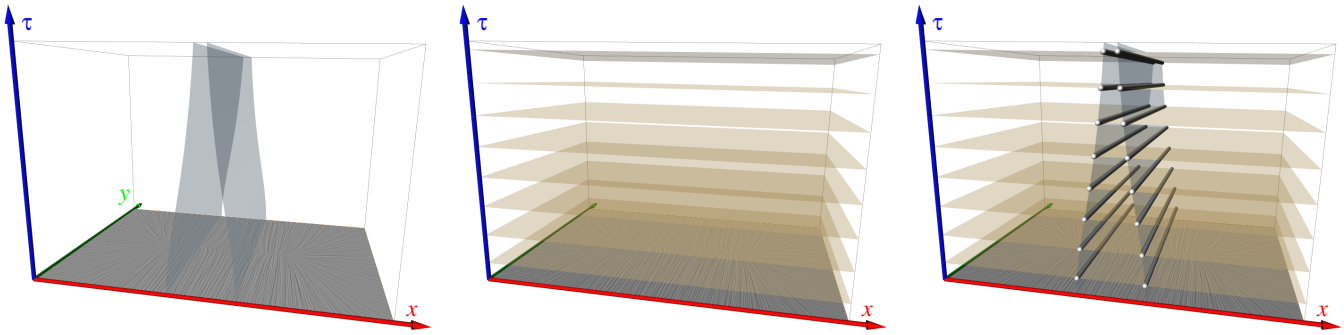

Figure 2: *In the* THREECP *flow, three critical points (sink, saddle, sink) are located on an attractor (see LIC slice on the ground). The left and middle images show zero-level isosurfaces of $\lambda_1(\mathbf{x},\tau)$ and $\lambda_2(\mathbf{x},\tau)$, respectively. These are locations from which inertial pathline integration leads to a singularity, i.e., intersecting trajectories. The intersection of the isosurfaces (gray lines in right image) shows locations, where nearby-released particles collapse onto a point.*

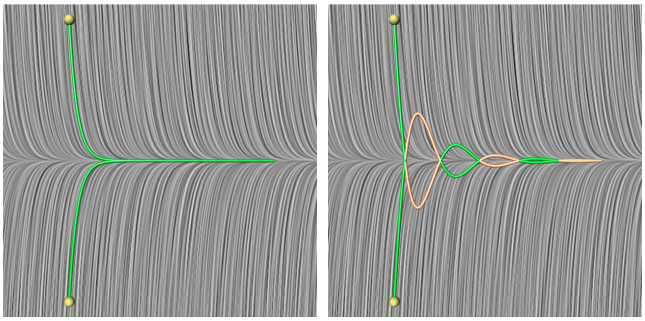

Figure 1: *Left: massless trajectories do not cross, right: inertial trajectories might intersect several times during convergence onto an attractor. In this figure, the sign of the determinant of the flow map gradient is color-coded (green: positive, orange: negative). As shown, the intersections are zero-crossings of the determinant.*

dimensional underlying flow, let $\lambda_1(\mathbf{x},\tau),\ldots,\lambda_n(\mathbf{x},\tau)$ be the eigenvalues of the inertial flow map gradient for each $(\mathbf{x},\tau)$. These are scalar fields in $(n+1)$-dimensional space-time. The determinant is likewise expressed as product of the eigenvalues:

$$\det(\,\phi_{\mathbf{x}}(\mathbf{x},\mathbf{v}_0,t_0,\tau)\,)=\prod_{i=1}^{n}\lambda_i \tag{6}$$

Therefore, Eq. (5) is fulfilled if any of the eigenvalues becomes 0. Thus, each eigenvalue scalar field $\lambda_i(\mathbf{x},\tau)$ contains zero-level isosurfaces from which an inertial pathline integration leads to a singularity. These isosurfaces are n-manifolds in space-time (e.g., for underlying 2D flows a surface in 3D space-time). If two isosurfaces intersect, i.e., if two eigenvalues become zero, an $n-1$ manifold arises in space-time (e.g., for underlying 2D flows a line in 3D space-time). An example is given in Fig. 2.

In 3D flows, three eigenvalues exist in 4D space-time, and they contain isovolumes (one eigenvalue is zero), isosurfaces (two eigenvalues are zero) or isolines (all three eigenvalues are zero).

3.1. Interpretation of Singularities

In the following, we examine how singularities can be interpreted. Singularities occur, when inertial trajectories cross. Conceptually, there are two kinds of crossings: a left/right switch and a front/back switch. In practice a combination of the two occurs. Left/right switches occur at attractors, as in Fig 1 (right), when inertial trajectories come in from opposite sides and oscillate around an attracting line. The front/back switch occurs when two particles move behind one another directly toward a sink, as in Fig. 2 (left). First, they will fly over it due to inertia, but will decelerate and return along the same path they came. When the particle in front starts to come back, the particle behind catches up and then moves past the one in front. (Regarding the LIC images, we assume in all examples a gravity-free environment, thus inertial critical points are at the same location as critical points of the underlying flow [GT16b].)

The types of switches cannot directly be associated with the eigenvalue fields by index. If the eigenvalues are equal, they might swap. This, however, is not critical, since we are only interested in the eigenvalues, when they are zero. The only potential swap of relevance is therefore when both become zero.

3.2. Multiple Singularities at the Same Observation

When recovering the origin of pollutants, we are interested in the set of seed points that lead inertial particles to the same observation, since each seed is a potential source of the observed pollution. In Fig. 1 (right), two crossing trajectories are shown, i.e., integration from two seed points leads to the same observation; in this case, a singularity. In this particular example, all locations on the line between the two highlighted seed points lead to the same singularity. Thus, for one observation point, there is an entire line of seeds leading to the observation after the *same* integration duration τ. Further, we already observed in Fig. 1 that trajectories intersect multiple times. Thus, for the observation point, there must be further lines of seeds (with different τ), for which the observation point is a later singularity along the trajectories. Fig. 3 visualizes all seed points from which an inertial pathline integration leads to the selected observation point (red). As can be seen, there is one seed line in each zero-level eigenvalue isosurface. In fact, the seeds are *only* located

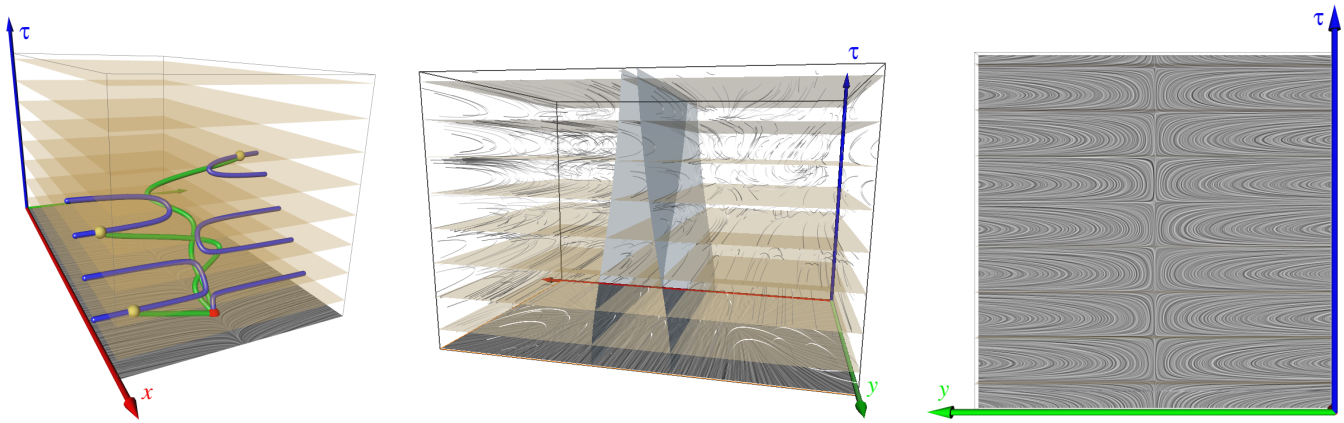

Figure 4: *Space-time visualizations of influence curves. Left: The influence curve (blue) of a single observation point (red) in the* ATTRACTOR *flow decays into multiple pieces. Inertial pathlines (green) reach the observation. Middle and right: A visualization of the influence curve vector field in the* THREECP *flow. The LIC slice shows that singularities (orange, transparent surfaces), act as poles of the influence curves.*

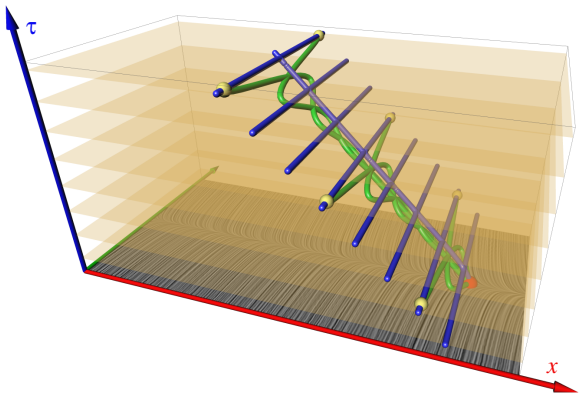

Figure 3: *Singularities in the* ATTRACTOR *flow (cf. Fig. 1) in space-time, whereas* τ *denotes integration duration. For a given observation point (red), all seeds are shown (blue lines) from which inertial pathline integration leads to the observation. A few exemplary inertial pathlines (green) were released from the yellow seed points, showing that they reach the observation point (red).*

on the eigenvalue isosurfaces (or directly on the attractor). Moving the red observation point, would also move the seed lines, thereby sweeping out the zero-level eigenvalue isosurfaces.

3.3. Singularities and Poles of Influence Curves

In the previous section, we considered sets of seed points, leading to the same observation. If the observation is exactly on an attractor, a ladder structure can appear as in Fig. 3, whereas each rung is on a zero-level eigenvalue isosurface. This means, there are sets of seed points that reach the observation after the *same* integration duration. If the observation is not on an attractor, there is only a single seed point for each integration duration. The union of these seed points thereby forms a curve that is parameterized by the integration duration. This curve is known as the influence curve [GT16c]. As can be seen in Fig. 4, the zero-level eigenvalue isosurfaces from which inertial pathline integration leads to singularities can act as poles of influence curves. Since influence curves may then exist on both sides of a pole, influence curves decay into pieces. An integration-based influence curve extractor can only extract curve segments between poles. Poles only occur, when there is an infinite number of seed points in the isosurface that lead after the *same* integration duration to the same singularity. This case is structurally unstable and therefore unlikely. Usually, influence curves may cross the isosurfaces in just a single point, as visible in Fig. 5. At the moment of the crossing, the inertial flow map gradient is singular and can thus not be inverted. Then, the influence curve vector field in Eq. (4) is undefined. Numerically, the integrator is likely to simply step over these undefined points. Care must be taken, though, since the influence curve vector field has high magnitude close to the zero-level eigenvalue isosurfaces. The next section is devoted to the influence curve extraction.

4. Influence Curve Extraction

In the following section, we revisit the integration-based approach to the influence curve extraction and reformulate the problem to provide a new extraction method.

4.1. Revisit the Tangent Curve Approach

First, we improve upon the original definition [GT16c] of the influence curve vector field $\mathbf{h}$, in which influence curves appear as tangent curves. Tracing influence curves in vector field $\mathbf{h}$ requires inversion of the spatial flow map gradient $\phi_{\mathbf{x}}$, cf. (4). This matrix inversion contains a division by the determinant $\det(\phi_{\mathbf{x}})$. Thus, when influence curves approach poles or zero-level eigenvalue isosurfaces, their tangent has extremely high magnitude, due to the division by the vanishing determinant, which makes numerical integration difficult. We found that a multiplication by the determinant in space-time is easier to integrate. Instead of extremely high magnitudes in space (the division by the determinant cancels out), the progress in time simply slows down. By using Eq. (4) we get:

$$\bar{\mathbf{h}}(\mathbf{x},t) = \frac{\mathrm{d}}{\mathrm{d}t}\begin{pmatrix}\mathbf{x}\\ t\end{pmatrix} = \det(\phi_{\mathbf{x}})\begin{pmatrix}\mathbf{h}(\mathbf{x},t)\\ 1\end{pmatrix} \tag{7}$$

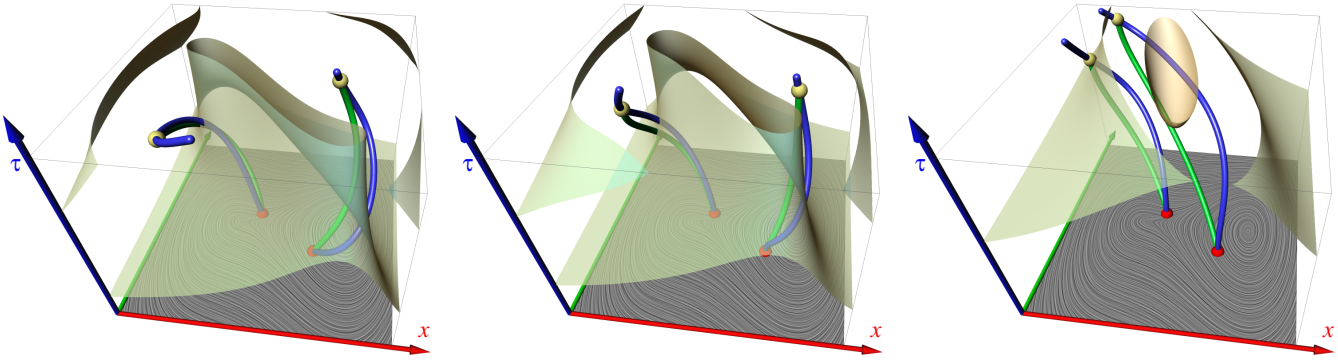

particle diameter: $d_p = 50\,\mu m$ particle diameter: $d_p = 200\,\mu m$ particle diameter: $d_p = 550\,\mu m$

Figure 5: *Zero-level eigenvalue isosurfaces in the* DUFFING *vector field for varying particle sizes. As shown, here, influence curves (blue) cross the isosurface. Inertial pathlines (green) released from the influence curve reach the observation point (red).*

This approach can be used to precompute the influence curve vector field, as done for the creation of the images in Fig. 4 (middle and right). In contrast to the next approach, this method allows for an accurate integration, as it offers the option to apply a predictor-corrector method on top [GT16c] in order to bound the integration error globally. On the other hand, the integration-based approach can only integrate a curve segment and cannot directly continue the integration on the other side of a pole, as it would be required to extract the blue influence curve segments shown in Fig. 4 (left).

4.2. Reformulation to Critical Line in Space-Time

We search for the union of seed points from which an inertial pathline integration leads to observation $\mathbf{x}$. In contrast to the previous section, we do not interpret the seeds as curves, parameterized by τ, since influence curves can degenerate when the inertial flow map gradient becomes singular, which might result in an infinite number of seed points existing for the same τ, cf. Section 3.3.

Given an observation $\mathbf{x}$, we compute for each seed point $\mathbf{x}_0$ and integration duration τ the difference vector $\mathbf{w}$ to the observation $\mathbf{x}$:

$$\mathbf{w}(\mathbf{x}_0, \tau) = \phi(\mathbf{x}_0, \mathbf{v}_0, t_0, \tau) - \mathbf{x} \tag{8}$$

where $\mathbf{w}(\mathbf{x}_0, \tau)$ can be interpreted as an unsteady vector field. We rearrange Eq. (3) and define the union of the $(n+1)$-D space-time seed points as set $\mathcal{C}$:

$$\mathcal{C} = \{(\mathbf{x}_0, \tau) \mid \mathbf{w}(\mathbf{x}_0, \tau) = \mathbf{0}\} \tag{9}$$

When influence curves are unique in the integration duration τ, influence curves can be extracted as paths of critical points in $\mathbf{w}(\mathbf{x}_0, \tau)$. In the degenerate case, when an infinite number of seed points exist per τ, the influence curves degenerate to a temporally-isolated critical line of $\mathbf{w}(\mathbf{x}_0, \tau)$.

In both cases, the resulting solution is a set of lines. For the case $n = 2$, we extract the seed line set $\mathcal{C}$ by intersecting the zero-level isosurfaces of the two components of vector field $\mathbf{w}$ (each component is a scalar field). The intersection retrieves locations in which both components, and therefore the vector $\mathbf{w}$ become zero. For $n = 3$, three isovolumes would have to be intersected, which also results in a set of curves.

This method is less accurate than the integration-based approach in Section 4.1, since we discretize vector field $\mathbf{w}(\mathbf{x}_0, \tau)$ to a certain resolution, prior to extraction and intersection of the isosurfaces. Moreover, the vector field $\mathbf{w}$ is different and has thus to be recomputed for every observation point $\mathbf{x}$. The method can, however, find degenerated (Fig. 3) and separated influence curve pieces (Fig. 4 (left)) in the presence of poles.

5. Implementation

In the following, we provide details regarding the extraction of singularities and influence curves.

5.1. Extraction of Singularities

In a preprocess, we discretized the spatio-temporal domain (resolution is given in Table 1) and performed a flow map integration at every seed point for several integration durations. Afterwards, we used central differences to approximate the spatial flow map gradients on the grid, and computed the eigenvalues λ_1 and λ_2 of the spatial flow map gradient. In addition, we create a filter field to mask out voxels, for which the inertial flow map has left the domain. Care must be taken to not write non-sense values into the eigenvalue fields, as they might lead to unwanted isosurfaces. The extraction and intersection of the respective isosurfaces, as well as the final visualization were done in Amira [SWH05].

5.2. Extraction of Influence Curves

For the space-time visualization of the influence curve vector field in Fig. 4 (middle and right), we sampled vector field $\bar{\mathbf{h}}$ according to Eq. (7). For the extraction of influence curves from this vector field, the usage of adaptive Runge-Kutta integrators is recommended [GT16c]. In this paper, we used the isosurface-based method from Section 4.2 to extract influence curves. As before, the required flow maps ϕ can be precomputed once, storing for each seed point $\mathbf{x}_0$, the resulting location after integration duration τ. We used the same resolution, given in Table 1. The difference vector $\mathbf{w} = \phi - \mathbf{x}$, and the isosurface extraction and intersection are then performed per (user-defined) observation point $\mathbf{x}$.

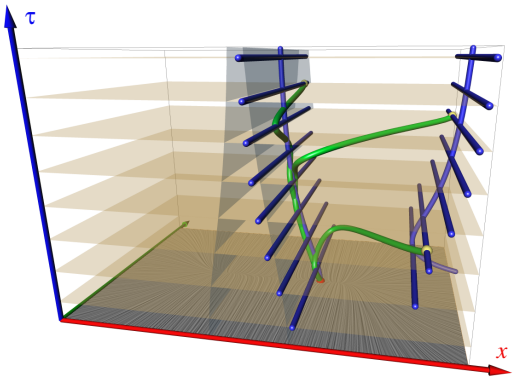

Figure 6: *Singularities in the* THREECP. *For the selected observation point (red), two lines of seed points (blue) exist in the zero-level eigenvalue isosurfaces (horizontal planes) of the inertial flow map gradient. Therefore, two ladder structures appear, from which inertial pathline integration (green lines) leads to the observation point. The observation point (red) is located on the attractor.*

6. Results

We extracted singularities and influence curves in three analytic and one sampled vector field. We begin with the analytic fields.

6.1. Attracting Line

In the previous sections, we used two vector fields to discuss singularities by example. The first vector field contains a simple attracting line at $y = 0$ on which all intersections of particle trajectories occur.

$$\mathbf{u}(x, y) = \begin{pmatrix} 1 \\ -10y \end{pmatrix} \tag{10}$$

We visualized and discussed the flow in the domain $D \times T = [0,8] \times [-2,2] \times [0,4]$ in Figs. 1, 3 and 4 (left). Since the flow goes constantly to the right, one of the eigenvalues remains constant $\lambda_1(\mathbf{x}, \tau) = 1$.

6.2. Three Critical Points on Attracting Line

The other main test case is the THREECP flow. This vector field similarly contains an attractor at $y = 0$, but here, three critical points are located on it, namely two sinks and a saddle in-between.

$$\mathbf{u}(x, y) = \begin{pmatrix} x(1-x)(1+x) \\ -10y \end{pmatrix} \tag{11}$$

This flow was visualized in the domain $D \times T = [-3,3] \times [-2,2] \times [0,4]$ in Figs. 2 and 4 (middle, right). In Fig. 6, all possible seeds for the selected observation (red) are shown. Since the observation is placed exactly on the attractor, the aforementioned ladder-type structures occur. Remarkably, there is not only one, but two such ladders, from which inertial pathlines (green) reach the observation.

6.3. Forced-Damped Duffing

The DUFFING vector field provides an example without an attracting line structure, but with two attracting points, i.e., two sinks. The vector field is analytically given as:

$$\mathbf{u}(x, y, t) = \begin{pmatrix} y \\ x - x^3 - 0.25y + 0.4\cos(t) \end{pmatrix} \tag{12}$$

in the spatial domain $D \times T = [-2,2]^2 \times [0,3]$. It is a time-dependent flow and was used by Haller and Sapsis [HS11] as testing ground for the computation of Lagrangian coherent structures and later by Günther and Theisel [GT15] to study finite-time mass separation. As shown in Fig. 5 for varying particle sizes, the zero-level eigenvalue isosurfaces are in most places identical (orange and blue surface overlap). This means, when inertial trajectories cross, they collapse onto a point. An exception can be seen in Fig. 5 (bottom), where a single orange isosurface exists at the top of the domain. This experiment demonstrates that influence curves can cross zero-level eigenvalue isosurfaces. At these crossing locations, the magnitude of the influence curve vector field vanishes. Further, singularities are mass-dependent, i.e., they depend on the particle response time r. Note that the response time depends on diameter d_p, density ρ_p and viscosity μ, cf. (2). Varying combinations of the three lead to the same response time, and therefore identical particle behavior.

6.4. Borromean

The BORROMEAN data set contains magnetic decaying rings and is courtesy of Candelaresi and Brandenburg [CB11]. We selected one slice of the domain, resulting in a 2D steady underlying vector field, in which we released inertial particles. Fig. 7 (left) shows the zero-level eigenvalue isosurfaces in space-time, and Fig. 7 (right) depicts one slice of it, showing the singularities at one particular integration duration. Especially in the slice, we notice two types of structures. Singularities either form ring-like shapes, especially around sinks, which corresponds to the aforementioned back-front switches, or the singularities form line-like shapes. The line-like shapes are closed curves that degenerated to a line, and due to the discrete sampling of the grid, the reconstructed surfaces suffer from sampling artifacts. Nevertheless, we can see in Fig. 7 (right) that the line-like shapes align along attracting structures in the flow, which makes sense and is expected, since inertial pathlines converge onto them and can intersect. Fig. 8 shows further singularity extraction results using different grid resolutions.

6.5. Performance

The inertial flows maps and eigenvalue fields were computed with double precision on an Intel Core i7-2600K CPU with 3.4 GHz and 24 GB RAM. The computation of flow maps is a massive inertial pathline tracing exercise and is easily parallelized with multithreading. The resolution of the flow map discretization as well as the extraction time of the eigenvalue fields, including the flow map computation, is given in Table 1. In all examples, the precomputation time was with $10-17$ seconds fairly small. The intersection of isosurfaces with Amira took in all our data sets roughly $2-5$ seconds. The exact time depends on the resolution of the underlying grid (which determines the size of the triangles to intersect) and the number of the triangles, i.e., the complexity of the isosurfaces.

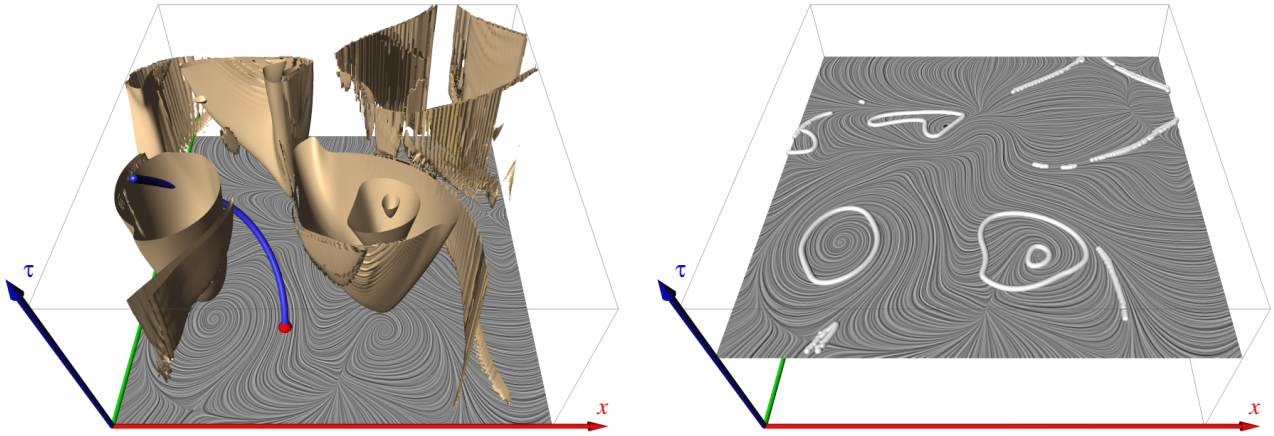

Figure 7: *Singularities in* BORROMEAN. *Left: Space-time view on zero-level eigenvalue isosurfaces, showing seeds from which inertial pathline integration leads to singularities. Starting from the observation point (red), the blue line depicts an influence curve that was extracted by the isosurface-based method. The influence curve intersects with one of the eigenvalue surfaces. Right: A time slice, containing zero-level isolines that are ring-shaped (around attracting critical points) or line-shaped (along attracting flow structures). A LIC visualization of the underlying vector field serves as context in the background. (Inertial structures align with the underlying flow since gravity is set to zero.)*

Data set	grid resolution	λ_i computation (secs.)
ATTRACTOR	$300 \times 200 \times 200$	9.9
THREECP	$300 \times 200 \times 200$	11.5
FORCED-DUFFING	$300 \times 300 \times 200$	14.9
BORROMEAN	$300 \times 300 \times 200$	16.4

Table 1: *Grid resolutions (space-time) and extraction timings of the eigenvalue scalar fields of the inertial flow map gradient.*

7. Conclusions

In this paper, we studied the crossings of inertial particle trajectories, i.e., singularities of the inertial flow map gradient. The sets of points, leading to a singularity, are n-manifolds in space-time, e.g., zero-level isosurfaces of the inertial flow map gradient's eigenvalue fields in 3D space-time. We discussed the meaning of singularities and the types of trajectory crossings. Further, we examined the relationship between singularities and influence curves, and found that the aforementioned isosurfaces can act as poles of influence curves. This has impact on influence curves in two ways: first, the original influence curve vector field can have high magnitude near the poles. We proposed a time-scaled formulation to avoid this. Second, influence curves may decay into disconnected pieces. To extract them all, we formulated influence curve extraction as critical point tracking problem, which we implemented on a discrete grid as the intersection of isosurfaces in space-time.

A limitation of the isosurface-based approach is that it involves discretization and requires a grid resolution to be set. In real-world flows with long integration time, discrete flow maps exhibit severe sampling issues such as aliasing [ÜSK*12]. Fig. 8 shows the impact of the resolution on the visual quality and extraction time of the singularities.

This paper gave new insights into the behavior and limits of techniques that require the inverse of the inertial flow map gradient, such as influence curves. An integration-based influence curve extraction works well, as long as the inertial flow map gradient stays positive-definite. In the future, we would like to speed up the search for influence curves in the alternative method and would like to use an adaptive representation of the inertial flow map to increase accuracy. Eventually, we would like to apply the new influence curve formulation to backward integration-based flow visualization techniques. In this paper, all examples visualized 2D flows, and we plan to experiment with 3D flows in the future.

Acknowledgements

This work was partially supported by DFG grant no. TH 692/13-1.

References

[Bor11] BORDÁS R.: *Optical measurements in disperse two-phase flows: Application to rain formation in cumulus clouds*. PhD thesis, University of Magdeburg, 2011. 1

[CB11] CANDELARESI S., BRANDENBURG A.: Decay of helical and nonhelical magnetic knots. *Phys. Rev. E 84* (2011), 016406. 6

[CST98] CROWE C., SOMMERFIELD M., TSUJI Y.: *Multiphase Flows with Droplets and Particles*. CRC Press, 1998. 2

[FH15] FARAZMAND M., HALLER G.: The Maxey–Riley equation: Existence, uniqueness and regularity of solutions. *Nonlinear Analysis: Real World Applications 22* (2015), 98–106. 2

[GKKT13] GÜNTHER T., KUHN A., KUTZ B., THEISEL H.: Mass-dependent integral curves in unsteady vector fields. *Computer Graphics Forum (Proc. EuroVis) 32*, 3 (2013), 211–220. 2

[GPPMn15] GARABOA-PAZ D., PÉREZ-MUÑUZURI V.: A method to calculate finite-time Lyapunov exponents for inertial particles in incompressible flows. *Nonlinear Processes in Geophysics 22*, 5 (2015), 571–577. 2

[GT14] GÜNTHER T., THEISEL H.: Vortex cores of inertial particles. *IEEE Trans. on Visualization and Computer Graphics (Proc. IEEE Scientific Visualization) 20*, 12 (2014), 2535–2544. 1, 2

[GT15] GÜNTHER T., THEISEL H.: Finite-time mass separation for comparative visualizations of inertial particles. *Computer Graphics Forum (Proc. EuroVis) 34*, 3 (2015), 471–480. 2, 6

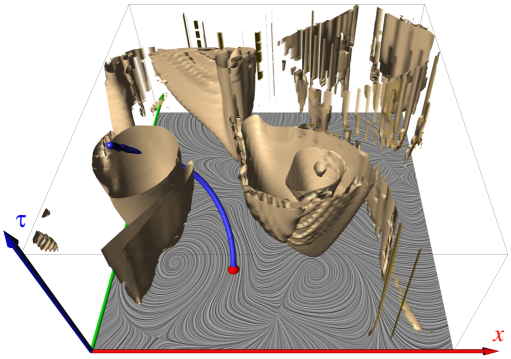

grid resolution: $100 \times 100 \times 100$ (1.9 sec.)

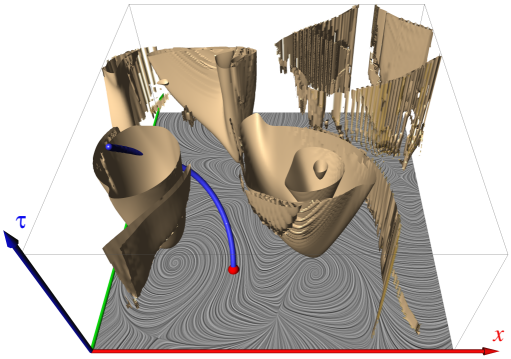

grid resolution: $200 \times 200 \times 200$ (8.7 sec.)

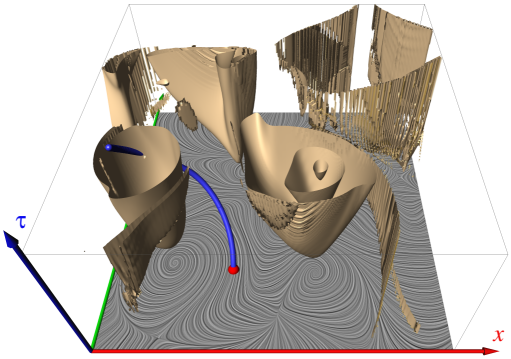

grid resolution: $300 \times 300 \times 300$ (18.0 sec.)

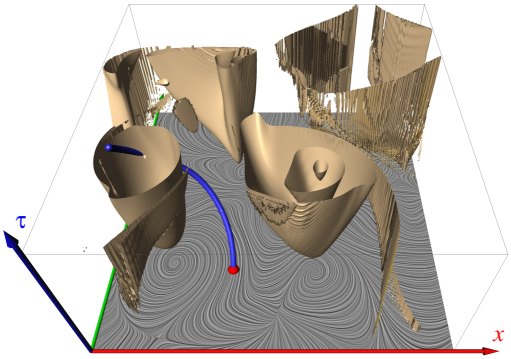

grid resolution: $400 \times 400 \times 400$ (45.6 sec.)

Figure 8: *Limitation: Sampling issues as seen with varying grid resolutions. Higher grid resolution results is longer extraction time.*

[GT16a] GÜNTHER T., THEISEL H.: Backward finite-time Lyapunov exponents in inertial flows. *IEEE Trans. on Visualization and Computer Graphics (Proc. IEEE Scientific Visualization)* (2016), to appear. 1, 2

[GT16b] GÜNTHER T., THEISEL H.: Inertial steady 2D vector field topology. *Computer Graphics Forum (Proc. Eurographics) 35*, 2 (2016), 455–466. 1, 2, 3

[GT16c] GÜNTHER T., THEISEL H.: Source inversion by forward integration in inertial flows. *Computer Graphics Forum (Proc. EuroVis) 35*, 3 (2016), to appear. 1, 2, 4, 5

[HS08] HALLER G., SAPSIS T.: Where do inertial particles go in fluid flows? *Physica D: Nonlinear Phenomena 237* (May 2008), 573–583. 1, 2

[HS11] HALLER G., SAPSIS T.: Lagrangian coherent structures and the smallest finite-time Lyapunov exponent. *Chaos 21*, 2 (2011), 023115. 6

[KGRK14] KUTZ B. M., GÜNTHER T., RUMPF A., KUHN A.: Numerical examination of a model rotor in brownout conditions. In *Proceedings of the American Helicopter Society* (May 2014), no. AHS2014-000343 in AHS 70th Annual Forum. 1

[MBZ06] MOGRABI E., BAR-ZIV E.: On the asymptotic solution of the Maxey-Riley equation. *Physics of Fluids 18*, 5 (2006). 1, 2

[MR83] MAXEY M. R., RILEY J. J.: Equation of motion for a small rigid sphere in a nonuniform flow. *Physics of Fluids 26*, 4 (1983), 883–889. 2

[PD09] PENG J., DABIRI J. O.: Transport of inertial particles by Lagrangian coherent structures: Application to predator–prey interaction in jellyfish feeding. *Journal of Fluid Mechanics 623* (3 2009), 75–84. 1, 2

[RRV14] RABEN S. G., ROSS S. D., VLACHOS P. P.: Experimental determination of three-dimensional finite-time Lyapunov exponents in multi-component flows. *Experiments in Fluids 55*, 10 (2014), 1–6. 2

[RSBE01] ROETTGER S., SCHULZ M., BARTELHEIMER W., ERTL T.: Automotive soiling simulation based on massive particle tracing. In *Data Visualization 2001*, Eurographics. Springer Vienna, 2001, pp. 309–317. 2

[SBL11] SYDNEY A., BAHARANI A., LEISHMAN J. G.: Understanding brownout using near-wall dual-phase flow measurements. In *Proceedings of the American Helicopter Society* (Virginia Beach, VA, May 2011), 67th Annual Forum. 1

[SBR15] SUDHARSAN M., BRUNTON S. L., RILEY J. J.: Lagrangian coherent structures and inertial particle dynamics. *ArXiv e-prints* (2015). 1512.05733. 2

[SGL10] SYAL M., GOVINDARAJAN B., LEISHMAN J. G.: Mesoscale sediment tracking methodology to analyze brownout cloud developments. In *Proceedings of the American Helicopter Society, 66th Annual Forum* (2010). 1

[SH09] SAPSIS T. P., HALLER G.: Inertial particle dynamics in a hurricane. *Journal of the Atmospheric Sciences* (2009). 1, 2

[SJJ*16] SAGRISTÀ A., JORDAN S., JUST A., DIAS F., NONATO L. G., SADLO F.: Topological analysis of inertial dynamics. *IEEE Transactions on Visualization and Computer Graphics (Proc. IEEE Scientific Visualization)* (2016), to appear. 2

[SPH11] SAPSIS T., PENG J., HALLER G.: Instabilities on prey dynamics in jellyfish feeding. *Bull Math Biol. 73*, 8 (2011), 1841–1856. 1, 2

[SRCV98] SHAW R. A., READE W. C., COLLINS L. R., VERLINDE J.: Preferential concentration of cloud droplets by turbulence: Effects on the early evolution of cumulus cloud droplet spectra. *Journal of the Atmospheric Sciences 55*, 11 (1998), 1965–1976. 1

[SWH05] STALLING D., WESTERHOFF M., HEGE H.-C.: Amira: A highly interactive system for visual data analysis. In *The Visualization Handbook*. Elsevier, 2005, pp. 749–767. 5

[ÜSK*12] ÜFFINGER M., SADLO F., KIRBY M., HANSEN C., ERTL T.: FTLE computation beyond first-order approximation. In *Eurographics (Short Papers)* (2012), pp. 61–64. 7

[WT10] WEINKAUF T., THEISEL H.: Streak lines as tangent curves of a derived vector field. *IEEE Transactions on Visualization and Computer Graphics (Proceedings Visualization 2010) 16*, 6 (2010), 1225–1234. 1